

# NON-LINEAR VORTEX BEHAVIOURS OF ROLLED SUPERSONIC TRANSPORT CONFIGURATION WITH LEADING-EDGE VORTEX FLAPS

Kenichi RINOIE\*, Masashi SHIROTAKE\* and Dong Youn KWAK\*\*

\* Department of Aeronautics and Astronautics,  
University of Tokyo, Tokyo, 113-8656, JAPAN

\*\* Japan Aerospace Exploration Agency, Tokyo, 181-0015, JAPAN

**Keywords:** *leading-edge flap, rolling moment, vortex interaction, SST*

## Abstract

Wind tunnel measurements were done to investigate the effect of leading-edge vortex flaps and leading-edge flaps on the rolling moment characteristics of the cranked arrow wing for the supersonic transport. Static rolling moment measurements, flow visualization studies and the cross flow velocity measurements by a particle image velocimetry were made at the Reynolds number based on the wing mean aerodynamic chord of  $6.2 \times 10^4$ . Static rolling moment measurements indicated linear restoring moment for the roll direction at incidence angles lower than about  $16^\circ$  for the entire model tested. When the outboard leading-edge flap is deflected  $12^\circ$ , rolling moment hystereses are observed at the roll angle of about  $20^\circ$  and at the incidence angle of about  $20^\circ$ . It was indicated that the hystereses are caused by different vortex breakdown behaviours on the inboard wing.

## Nomenclature

$b_{\max}$	wing maximum span length, m
$C_{\text{mac}}$	wing mean aerodynamic chord, m
$C_r$	wing root chord at model centre-line, m
$C_{\text{rol}}$	rolling moment coefficient non-dimensionalized using $b_{\max}$ measured about body axis $x$
$L/D$	lift/drag ratio
$Re$	Reynolds number based on mean aerodynamic chord
$U_\infty$	free stream velocity, m/s
$v$	mean velocity in $y$ direction

$w$	mean velocity in $z$ direction
$w_b$	mean velocity in $z_b$ direction
$x$	chordwise coordinate measured from apex of delta wing at model centre-line, m
$y$	horizontal coordinate orthogonal to $x$ , measured from model centre-line, m
$y_b$	spanwise coordinate orthogonal to $x$ , fixed to the body and measured from model centre-line, m
$z$	coordinate orthogonal to $x$ and $y$ measured from model centre-line, m
$z_b$	coordinate orthogonal to $x$ and $y_b$ measured from model centre-line, m
$\alpha$	wing angle of attack, degree
$\delta_{\text{flE}in}$	inboard vortex flap deflection angle, degree
$\delta_{\text{flE}out}$	outboard leading-edge flap deflection angle, degree
$\phi$	roll angle, degree (clockwise direction is positive when seen from downstream of the model)
$\theta$	incidence angle, degree
$\xi$	vorticity in $y$ - $z$ plane, see eq. (1)

## 1 Introduction

A delta wing planform is often used for high speed aircraft such as a supersonic transport (SST) because of its good supersonic performance. Since the aspect ratio of the delta wing is relatively small, the lift curve slope of the delta wing is also low and hence the delta wing aircraft has to fly at a high angle of attack at low speeds such as at take-off and landing. At

high angles of attack, a pair of leading-edge separation vortices is formed on the delta wing and produces a suction force over the wing which increases the lift component. However, there is also a high drag component associated with the suction force.

When the delta wing aircraft flies at high angles of attack, the delta wing sometimes experiences a self-induced roll oscillation known as a wingrock [1]. The wingrock originates from the unstable rolling moment caused by the behaviours of the leading-edge separation vortex such as a vortex interaction and a vortex breakdown. Even when the delta wing is rolled statically, the effective sweepback angle on the windward wing is different from that of the leeward wing [1]. This asymmetry induces the asymmetric formation of the leading-edge vortices and the wing exhibits complex aerodynamic behaviours. Therefore, static rolling moment characteristics are one of the important factors for the aerodynamic design of delta wing aircrafts.

In the case of the main wing of the supersonic transport configuration, it has either a double delta wing or a cranked arrow wing. They have a different leading-edge sweepback angle at the inboard and outboard leading edges. Two pairs of leading-edge separation vortices are formed both on the inboard and outboard wings. These vortices interact with each other and the wing characteristics are different from that of the plain delta wing [2, 3]. Static roll characteristics of these wings could also be different from that of the delta wing due to a complex behaviour of the vortices. However, as far as the authors know, there are only a few references on the static roll characteristics of either the double delta wing or the cranked arrow wing [4].

The lift/drag ratio ( $L/D$ ) at low speeds is an essential factor for the improvement of the take-off and climb performance of the SST. The  $L/D$  of the delta wing aircraft is relatively poor, because of the high drag as mentioned above. To improve the lift/drag ratio of the delta wing, a leading-edge device called a leading-edge vortex flap is used for a highly swept-back delta wing [5]. It is a full span deflectable surface at

the leading-edge of the delta wing that utilizes the suction force generated by the vortex formed on the deflected flap surface to reduce the drag and to improve the lift/drag ratio. The first author has made several experimental studies on vortex flaps for delta wing configurations that have different flap leading-edge shapes and different flap planforms [6-9] to discuss the optimum vortex flap configurations.

As for the SST configuration, the vortex flap and the leading-edge flap can be used for the inboard wing and the outboard wing, respectively, because the inboard wing has a higher sweepback angle and the outboard wing a lower sweepback angle. Therefore, in ref. [10], authors applied the leading-edge vortex flaps and the leading-edge flaps on the cranked arrow wing SST configurations. Results indicated that the combination of the leading-edge vortex flaps at the inboard wing and the leading edge flaps at the outboard wing shows a high lift/drag ratio benefit in a wide lift coefficient range.

It is of interest to see how the deflection of vortex flaps and leading-edge flaps affect the rolling moment characteristics of the cranked arrow SST wing. Static rolling moment measurements for the SST with vortex flaps and leading-edge flaps have been carried out in ref. [11]. Results indicated a nonlinear and abrupt change of rolling moments when the flaps were deflected. However, details of the vortex behaviour that affect the rolling moment characteristics were not clarified.

In this paper, experimental studies using a particle image velocimetry (PIV) have been made to reveal this complex vortex behaviour that causes the nonlinear and abrupt change of static rolling moments for the SST model with vortex flaps and leading-edge flaps.

The SST configuration used in this study is of a smaller scale but similar in planform configuration as used in refs. [10] and [11]. It is based on the cranked arrow wing configuration that was designed for the supersonic flight test programme, which is currently underway at the Japan Aerospace Exploration Agency. The leading-edge of this wing was modified so that it has vortex flaps for the inboard section and leading-edge flaps for the outboard section.

Experiments were conducted in a 0.6m x 0.6m blow-down low speed wind tunnel. The Reynolds number based on the mean aerodynamic chord was  $6.2 \times 10^4$ . PIV measurements were conducted to investigate the flap deflection effects on the static rolling moment characteristics in detail.

In summary, the purpose of this study is to discuss the effect of leading-edge flap and vortex flap deflections on the static roll characteristics of the cranked arrow SST configuration and to clarify the complex and non-linear behaviour of the leading-edge separation vortices formed on the wing.

## 2 Experimental Details

Figure 1 shows the model details. This SST configuration model is based on the cranked arrow wing configuration with a fuselage section that was preliminary designed for the supersonic flight test programme conducted by the Japan Aerospace Exploration Agency [12]. The present wind tunnel model is 1/5 scale of the original wind tunnel model. Although the original model used in [10] had a warped wing section, the current model wing is a flat plate and its thickness is 0.001m. The upper and lower surfaces of all of the edges are beveled. The wing has a sweepback angle of  $66^\circ$  at the inboard section and  $42^\circ$  at the outboard section. The kink is located between the inboard and outboard wings at  $y/(b_{\max}/2) = 0.55$ . The leading-edge of this model was modified so that it has the vortex flaps on the inboard wing and the leading-edge flaps on the outboard wing (Fig.1). Since the sweepback angle of the inboard wing is large, the inboard leading-edge flap has been thought to act as the vortex flaps. The chord length of this inboard vortex flap is  $0.1C_{\text{mac}}$ . The chord length of the outboard leading-edge flap is 20% of the local chord length at each spanwise station. The vortex flap deflection angle  $\delta_{\text{fLEin}}$  for the inboard wing is defined as the angle measured in the plane that is normal to the hinge line. The leading-edge flap deflection angle  $\delta_{\text{fLEout}}$  for the outboard wing is defined as the angle measured parallel

to the free stream. The tested flap deflection angles are  $\delta_{\text{fLEin}} = 0^\circ, 30^\circ$  and  $\delta_{\text{fLEout}} = 0^\circ, 12^\circ$ . The flaps have been designed so that there is no gap between the inboard leading-edge flap and the outboard leading-edge flap at the kink when  $(\delta_{\text{fLEin}}, \delta_{\text{fLEout}}) = (30^\circ, 12^\circ)$ . The nose section of the fuselage, that is 25% of the total fuselage length, is an ogive-cone-cylinder.

The experiments were made in a 0.6m x 0.6m blow-down type low-speed wind tunnel at the University of Tokyo. Tests were made at a tunnel speed of  $U_\infty = 10\text{m/s}$  except where noted. The Reynolds number based on the mean aerodynamic chord ( $C_{\text{mac}} = 0.087\text{m}$ ) was  $Re = 6.2 \times 10^4$ . The incidence angle  $\theta$  was in a range from  $0^\circ$  to  $+30^\circ$ . (This angle is equal to the angle of attack when the roll angle  $\phi = 0^\circ$ .) Rolling moment was measured using a two-component balance. The model was attached to the balance with a sting and can be rotated around its centre axis with balance using a stepping motor. The rolling moment is the roll component around the model centre axis (Fig. 2). The rolling moment coefficient  $C_{\text{roll}}$  has been obtained by rolling the model at  $2^\circ$  increments from  $\phi = -30^\circ$  to  $+30^\circ$  and by rolling back from  $\phi = +30^\circ$  to  $-30^\circ$  which consists of one cycle of the measurements. The model is at rest at each prescribed roll angle  $\phi$  for about 3.5sec, while the rolling moment measurements were conducted. This measurement was repeated for 10 cycles and the mean value of  $C_{\text{roll}}$  was obtained. The definition of  $C_{\text{roll}}$  is indicated in Fig. 2. The definition of the  $x, y, z$  coordinate system used here is also indicated in Fig.2. Please note that the  $x, y$  and  $z$  systems are dependent of the model incidence angle but independent of the model roll angle. All of the aerodynamic coefficients were calculated based on the original wing area without any flap deflection. The estimated overall accuracy of the aerodynamic coefficients is, at most,  $\pm 2\%$ .

Examples of the notation used in this paper are as follows. S001200 is the original wing with  $\delta_{\text{fLEin}} = 0^\circ$  and  $\delta_{\text{fLEout}} = 12^\circ$ . The last two digits of this notation are reserved for the trailing-edge flap.

The PIV system used here was DANTEC PIV 2000 Flowmap system with 50mJ dual cavity Nd:Yag lasers. Mist made of Ondina oil was used to seed the wind tunnel. The two-dimensional velocity distributions ( $v$ ,  $w$ ) in the  $y$ - $z$  plane normal to the model centre axis  $x$  were measured at different chordwise stations. PIV measurements were repeated for 2 planes within the flow field over the left wing when measured at a chordwise station of  $x=0.83Cr$ . Typical measurement plane size was about  $0.04 \times 0.04\text{m}^2$  which resulted in  $62 \times 62$  velocity vectors in every plane. The flow over the right wing at the roll angle of  $\phi$  was assumed to be the same for the flow over the left wing at the roll angle of  $-\phi$ . Measurements were repeated 300 times at each plane with a velocity acquisition rate of 7.5Hz. Intervals of two laser pulses were set to be  $25\mu\text{s}$ . The standard data validation method recommended in [13] was applied to the measured data. Mean velocities were obtained as ensemble averages. The overall accuracy of the mean velocity is  $\pm 6\%$  based on the error estimation method in [14]. Vorticity  $\xi$  has been estimated using the measured velocity data ( $v$ ,  $w$ ).  $\xi$  is defined by

$$\xi(m, n) = \{w(m+1, n) - w(m-1, n)\} / \Delta y - \{v(m, n+1) - v(m, n-1)\} / \Delta z \quad (1)$$

where  $\xi(m, n)$  is the vorticity at grid position ( $m$ ,  $n$ ), and  $\Delta y$ ,  $\Delta z$  are the grid spacing in the  $y$  and  $z$  directions (velocity data are given on a discrete grid in the PIV measurement plane).  $\xi$  is nondimensionalized by  $U_\infty$  and  $C_{mac}$ .

Since some CCD sensor pixels of the CCD camera used for the PIV measurements (light sensitive pixel number of the CCD camera:  $1008 \times 1018$ ) have been damaged accidentally, the correct velocity distributions could not be obtained around these sensor pixel areas. These areas are indicated in the ovals in the PIV results (eg. see Figure 4).

When the PIV measurements and the balance measurements are conducted at the same time (please refer to 3.2.2), the model was rolled in the same manner as the balance measurements described above. While the model is at rest at each  $\phi$ , the velocity

acquisition made by the PIV were conducted to obtain 5 pictures. By repeating the roll cycle ( $\phi = -30^\circ \rightarrow +30^\circ \rightarrow -30^\circ$ ) for 60 times, 300 pictures were obtained for each  $\phi$  and the averaged velocity distributions were obtained.

Smoke flow visualization tests were conducted to describe the flow around the model. The oil mist used for the PIV measurements was also used to visualize the flow. The light sheet used to illuminate the flow was normal to the  $x$  axis. The smoke visualization picture was taken from downstream of the model. Smoke visualization tests were conducted at  $U_\infty = 7\text{m/s}$  to improve the smoke density inside the flow. Oil flow visualization tests were also made to describe the surface flow pattern.

### 3 Results and Discussion

#### 3.1 Original Wing without Flap Deflection

In this section, the performance of the original wing without flap deflection is summarized and discussed. Figure 3 shows the results of static rolling moment characteristics  $C_{roll}$  versus roll angle  $\phi$  for different incidence angles  $\theta$  without flap deflection (S000000). The mean rolling moment when the roll angle  $\phi$  was increased from  $-30^\circ$  to  $+30^\circ$  and when  $\phi$  was decreased from  $+30^\circ$  to  $-30^\circ$  are indicated separately. This figure shows that the linear restoring (stable) moment for the roll direction is acting on the wing at the incidence angles  $\theta$  of  $12^\circ$  and  $14^\circ$ . As explained in [15] for the wing at relatively low incidence angles, decrease in the effective sweepback angle on the leeward wing and increase in this angle on the windward wing cause the restoring moment when the roll angle of the delta wing is increased. As the incidence angle is increased, the linearity observed at lower  $\theta$  is gradually lost. At  $\theta = 26^\circ$ ,  $C_{roll}$  indicates both the restoring and the unstable rolling moment distributions alternately. At  $\theta = 28^\circ$ ,  $C_{roll}$  drastically changes its state to an unstable one. This unstable characteristic is also observed at  $\theta = 30^\circ$ . According to [16], abrupt changes in the rolling moment at higher

incidence angles are attributed to asymmetric vortex breakdown.

Figure 4 shows the cross flow velocity and vorticity distributions over the wing measured by the PIV for S000000 configuration at the incidence angle  $\theta$  of  $20^\circ$  and at 83% root chord ( $x=0.83Cr$ ). The measured roll angles are  $\phi=0^\circ$ ,  $10^\circ$  and  $20^\circ$ . Smoke flow pictures taken at the same configurations are also shown. In this paper the number of velocity vectors has been reduced to  $21 \times 21$  vectors for easiness in viewing the results. At  $\phi=0^\circ$  (Fig.4a, left wing only), the formations of inboard vortex ( $y/C_{mac}=-0.4$ ) and outboard vortex ( $y/C_{mac}=-0.7$ ) are clearly visible. The outboard vortex originates from the kink of the cranked arrow wing. As the wing is rolled to  $\phi=10^\circ$  and  $20^\circ$ , the absolute value of the vorticity  $\xi$  increases at the centre region of the inboard vortex on the leeward wing (left wing) and the vortex core is clearly visible in the visualized picture when  $\phi=20^\circ$ . The wing roll increases the effective sweepback angle on the leeward wing that causes the vortex breakdown location to move toward the trailing edge and that creates stronger vortices upstream of the breakdown point [16].

Figure 5 shows the results for S000000 configuration at  $x=0.55Cr$  when  $\theta=20^\circ$  and  $\phi=20^\circ$ . Since the measured cross plane were located upstream of the outboard wing, the outboard vortex is not observed.

Figure 6 shows the results for S000000 configuration at  $\theta=26^\circ$  and at  $x=0.83Cr$  when  $\phi=20^\circ$ . The vorticity of the inboard vortex is much smaller than that at  $\theta=20^\circ$ ,  $\phi=20^\circ$  (Fig.4c). This indicates that large vortices, that have already been broken-down, are formed on this configuration. The outboard vortices on the windward and leeward wings are located much further away from the wing surface when compared to the results at  $\theta=20^\circ$ ,  $\phi=20^\circ$ .

### 3.2 Wing with Outboard Flap Deflection

In this section, the performance of the cranked arrow wing with the outboard leading-edge flap deflection is discussed.

#### 3.2.1 Overall Characteristics

Figure 7 shows the results of  $C_{roll}$  versus  $\phi$  for different  $\theta$  with the outboard flap deflection of  $\delta_{flEout}=12^\circ$  (S001200). This figure indicates a linear restoring rolling moment until  $\theta=16^\circ$ . Nonlinear rolling moment characteristics are seen at  $\theta$  higher than  $18^\circ$ . Both the restoring and the unstable rolling moment distributions are observed alternately at  $\theta=28^\circ$ . The unstable static roll characteristic is observed for all the measured roll angles at  $\theta=30^\circ$ . Furthermore, at  $\theta=20^\circ$ , rolling moment hystereses are observed at the roll angle of  $\phi=\pm 20^\circ$  and  $\pm 22^\circ$  (i.e. different rolling moment is measured when the model is rolled in the clockwise direction (from  $\phi=-30^\circ$  to  $+30^\circ$ ) and in the counter-clockwise direction (from  $\phi=-30^\circ$  to  $+30^\circ$ ) when seen from downstream of the model). Similar static rolling moment hystereses have been observed for the  $65^\circ$  and  $80^\circ$  delta wings [17, 18].

Figure 8 shows the cross flow velocity and vorticity distributions over the wing for S001200 configuration at the incidence angle  $\theta$  of  $20^\circ$  and at  $x=0.83Cr$  together with the smoke visualization pictures. The results at  $\phi=0^\circ$  are shown in Fig.8a. When compared to the results in Fig. 4a, it can be said that the deflection of the outboard wing has little effect on the formation and location of the inboard primary vortex. However, the outboard vortex ( $y/C_{mac}=-0.7$ ) is located much closer to the surface and much further away from the inboard vortex when compared to S000000 because of the outboard flap deflection. Figure 8b shows the results at  $\phi=10^\circ$ . This figure shows that the outboard vortices formed both on the windward and leeward wings are still located closer to the surface than that of S000000 at the same condition (Fig.4b). Furthermore, the absolute values of the vorticity at the centre of the outboard vortices for S001200 are slightly higher than those for S000000. Figure 8c shows the results for S001200 at  $\phi=20^\circ$ . Similar tendency to that at  $\phi=10^\circ$  is observed.

#### 3.2.2 Rolling Moment Hystereses

The rolling moment hystereses cannot be discussed from Fig.8c, because each PIV

measurement at different roll angles was done independently. It has been thought that the PIV measurements should also be conducted in a similar manner to those of the rolling moment as described in the Experimental Details. Figures 9 and 10 show the cross flow velocity and vorticity distributions over the wing for S001200 configuration at  $\theta=20^\circ$  and at  $x=0.83Cr$  together with the smoke visualization pictures, when the PIV measurements were conducted as described above. Figure 9 is the results at  $\phi=18^\circ, 20^\circ, 22^\circ$  and  $24^\circ$  when the model is rolled in the clockwise direction seen from the downstream of the model. Figure 10 is the results when the model is rolled in the counterclockwise direction. It must be noted that the measurements were done from  $\phi=-30^\circ$  to  $+30^\circ$  in Fig. 9 and from  $\phi=+30^\circ$  to  $-30^\circ$  in Fig. 10 to conduct the measurements at the same condition as the rolling moment measurements.

Figures 9a and 10a indicate that there are almost no differences between the PIV results in the clockwise rotation and those in the counterclockwise rotation at the same roll angle of  $\phi=18^\circ$ . Figures 9d and 10d also indicate no difference between the two at  $\phi=24^\circ$ . However, at  $\phi=20^\circ$  and  $22^\circ$ , differences are observed in the inboard vortex on the leeward wing between the results in the clockwise rotation and in the counterclockwise rotation when compared to either the set of Fig.9b and Fig.10b or the set of Fig.9c and Fig.10c. When the model is rolled in the counterclockwise direction (Figs. 10b and 10c), the inboard vortex core on the leeward wing is clearly visible in the velocity distributions (i.e. high vorticity at the vortex core) and in the smoke pictures. On the other hand, according to the results in the clockwise direction (Figs. 9b and 9c), the vortex core of the inboard vortex on the leeward wing is not clearly visible and the absolute value of vorticity at the outboard vortex is lower than that of Figs. 10b and 10c. As for the windward wing, the inboard vortices of all of the figures show almost the similar distributions. This means that the flow is not affected by the difference in the rolling direction on the windward wing at  $\phi=20^\circ$  and  $22^\circ$ .

From the results in Figs. 9 and 10, it can be summarized that the inboard vortex on the leeward wing tends to keep the amount of vorticity at the vortex core high, i.e. the vortex does not break down until at a lower roll angle when the model is rolled in the counterclockwise direction (Fig.10b and 10c) than when the model is rolled in the clockwise direction (Fig. 9b and 9c). This means that the chordwise position of the vortex breakdown of the inboard vortex on the leeward wing is affected by the roll directions.

Here we compare the rolling moment results shown in Fig. 7 to the PIV measurements in Figs. 9 and 10. The triangular symbol at  $\phi=20^\circ$  when  $\theta=20^\circ$  in Fig.7 corresponds to the PIV results in Fig. 9b and the rectangular symbol at  $\phi=20^\circ$  corresponds to the PIV results in Fig. 10b. The inboard vortex on the leeward wing when rolled in the counterclockwise direction has a higher absolute value of vorticity than that when rolled in the clockwise direction, as was seen in Figs. 9b and 10b. Therefore, in this case, the rolling moment stability has decreased. The absolute value of  $C_{roll}$  is smaller than that in the clockwise direction, as was shown by the rectangular symbol at  $\phi=20^\circ$  in Fig. 7.

As noted in the Experimental Details section, the present measurements were done by rolling the model at  $2^\circ$  increments between  $\phi=-30^\circ$  and  $+30^\circ$ . The model stopped rolling at each prescribed roll angle and stayed still for about 3.5sec, while the rolling moment and PIV measurements were conducted. This measurement was repeated for 10 cycles and the mean value of  $C_{roll}$  was obtained. Here, additional rolling moment measurements were done by doubling this stationary time at each roll angle. The measured results still indicated the rolling moment hystereses very similar to the one observed in Fig. 7.

Figure 11 shows the velocity distributions inside the inboard vortex at  $\theta=20^\circ$  and at  $x=0.83Cr$  for  $\phi=18^\circ, 20^\circ, 22^\circ$  and  $24^\circ$  when rolled either in the clockwise or in the counterclockwise directions. The velocity distributions  $w_b$  along the line that is parallel to

the  $y_b$  axis are indicated (please see an explanatory sketch of this figure). This line includes the vortex centre position for the inboard vortex on the leeward wing. The centre of the vortex location was determined from the measured velocity distributions by PIV when  $v_b=0$  and  $w_b=0$  ( $v_b$  is the velocity component parallel to the  $y_b$  axis). Fig. 11 shows that the velocity distributions  $w_b$  when rolled in the clockwise direction are relatively similar to those when rolled in the counterclockwise direction at  $\phi=18^\circ$ . The same tendency is seen at  $\phi=24^\circ$ . However, at  $\phi=20^\circ$  and  $22^\circ$ , absolute values of  $w_b$  when rolled in the counterclockwise direction is much higher than those when rolled in the clockwise direction. The higher absolute value of velocity means a strong velocity gradient at the centre of the vortex which is a typical feature of the leading-edge separation vortex before breakdown [19]. On the contrary, the decrease in velocity gradient near the core region is the feature of the vortex breakdown [20]. Therefore, the observed velocity difference between the clockwise and counterclockwise rotation at  $\phi=20^\circ$  and  $22^\circ$  comes from the fact whether the vortex has been broken down (lower velocity gradient of  $w_b$ ) or not (higher velocity gradient of  $w_b$ ). These results confirm the observations discussed in Figs. 9 and 10.

### 3.2.3 Discussion

Figure 12 shows the oil flow visualization pictures together with the smoke flow visualizations at  $x/Cr=0.55, 0.7, 0.77$  and  $0.83$  for the S000000 and S001200 at  $\theta=20^\circ, \phi=0^\circ$ . Results of both wings clearly indicate similar formation of the inboard vortex. However the smoke visualization tests suggest that the inboard vortex has been broken down at  $x/Cr=0.77$  for S001200 while the inboard vortex for S000000 has a vortex core at the same chordwise station. The oil flow patterns over the outboard wing are different for the two wings. For S001200, because of the outboard leading-edge flap deflection, the core diameter of the outboard vortex is small when compared to that of S000000 (see smoke picture at  $x/Cr=0.83$  for

S000000). The smoke flow visualization picture of S000000 (Fig.12a) indicates that the outboard vortex and the inboard vortex are located very near each other for S000000. This means that the two vortices interact with each other. Ref. [2] discussed that the vortex interaction on the delta wing has a stabilizing effect with respect to the vortex breakdown. The difference of interaction between the inboard and the outboard vortices for S000000 and S001200 has affected the vortex breakdown position for these two configurations.

Figure 13 shows the observed chordwise position of the vortex breakdown for the inboard vortex formed on the left wing. Results of S000000 at  $\theta=20^\circ, 26^\circ$  and those of S001200 at  $\theta=20^\circ$  are shown. The breakdown positions were determined with the aid of the smoke flow visualization by observing the light sheet normal to the  $x$  axis located at different chordwise positions. Since the vortex breakdown position is not steady and exhibits fluctuations along the axis of the vortices [21], positions where the vortex core is clearly visible (closed symbol) and where the core is not visible at all (open symbol) are indicated in this figure. It is thought that the breakdown occurs between these positions. Furthermore, to make the observation easy, the freestream velocity was decreased to  $U_\infty=5\text{m/s}$  in this observation.

Figure 13 indicates that the breakdown position on the windward wing ( $\phi<0$  on left wing) is relatively insensitive to the roll angle. This figure also shows that the breakdown position of S001200 is located upstream of that of S000000 at  $\theta=20^\circ$  as discussed in Fig.12. On the leeward wing of S001200, the breakdown position rapidly moves from about  $x/Cr=0.85$  to the trailing-edge at about  $\phi=20^\circ$ . This rapid movement of the breakdown position near the trailing-edge was also observed on the delta wings that have different sweepback angles [22]. Figure 7 indicated that there are rolling moment hystereses at this roll angle. Ref. [17] discussed that the hystereses, observed for the delta wing, are caused by the vortex breakdown location rapidly crossing the trailing-edge. This agrees with the observations for S001200 in Fig.13.

Similar rapid movement of breakdown near the trailing-edge is also observed for S000000 at  $\theta=26^\circ$  near  $\phi=30^\circ$ . However, the rolling moment hystereses were not observed at this configuration as was shown in Fig.3. Figure 12 indicated that the inboard and outboard vortices are merging into one vortex at  $\theta=20^\circ$ ,  $\phi=0^\circ$ . Comparisons between Fig.4c (S000000) and Fig.8c (S001200) indicated that the outboard vortices are located much nearer to the inboard vortex for S000000 at  $\theta=20^\circ$  when  $\phi=0^\circ$ ,  $10^\circ$  and  $20^\circ$  at  $x/Cr=0.83$ . These results suggest that the inboard and outboard vortices are merging into a single vortex on the S000000 wing near this chordwise station. When the two vortices are located relatively near such as on the  $76^\circ/40^\circ$  double delta wing [23], it is reported that the breakdown of the inboard vortex is triggered by the burst of the outboard vortex. It is thought that the inboard and outboard vortices formed on S000000 affected each other in a similar manner to those formed on the wing in [23]. This may have a possibility to preclude the rolling moment hystereses for S000000. On the contrary, since two vortices on S001200 behave independently, the rolling moment hystereses were observed that is quite similar to those for delta wings [17,18].

Another rolling moment characteristics that should be specially mentioned in Fig.7 is that at  $\theta=18^\circ$  and  $20^\circ$  the slope of the  $C_{roll}$  versus  $\phi$  curve is locally positive near  $\phi=0^\circ$ . This locally unstable  $C_{roll}$  slope at  $\phi=0^\circ$  was also observed at  $65^\circ$  delta wing at the incidence angle higher than  $30^\circ$  [24]. Ref. [24] discussed that the movement of vortex breakdown generates a statically unstable  $C_{roll}$  slope at  $\phi=0^\circ$ . However, as Fig.13 indicates, the movement of vortex breakdown location is very small near  $\phi=0^\circ$ . Further investigation is necessary to clarify this phenomenon.

As described before, the tested Reynolds number based on  $C_{mac}$  was  $Re=6.2 \times 10^4$ . Refs. [25] and [26] investigated the sensitivity of the Reynolds number on the double delta wing performance. Although the effect of Reynolds number on the force measurements is small, the inboard and outboard vortices are coiled-up at

low Reynolds number, but they remain separated at high Reynolds number [26]. The reported critical Reynolds number based on the root chord in [26] was the order of  $10^4$  and it was dependent on the wing leading-edge sweepback angle. This suggests that both the flow around the present SST configuration and the rolling moment hystereses observed in this paper may be dependent on the Reynolds number. Further investigation is also necessary to clarify the effects of Reynolds number on the SST static roll characteristics and the rolling moment hysteresis.

### 3.3 Wing with Inboard Vortex Flap Deflection

In this section, the performance of the cranked arrow wing with inboard vortex flap deflection is summarized. Figure 14 shows the results of  $C_{roll}$  versus  $\phi$  for different  $\theta$  with vortex flap deflection of  $\delta_{flE\text{in}}=30^\circ$  (S300000). This figure indicates that overall tendency of  $C_{roll}$  at  $\theta \leq 20^\circ$  is relatively similar to that of S000000 (Fig.3). At  $\theta > 20^\circ$ ,  $C_{roll}$  indicates both the restoring and the unstable rolling moment distributions alternately as in the S000000 wing at  $\theta=26^\circ$ .

Figure 15 shows the cross flow velocity and vorticity distributions over the wing for S300000 configuration at the incidence angle  $\theta$  of  $20^\circ$  at  $x=0.55Cr$  and  $0.83Cr$ . When compared to the results in Fig.5 and Fig.15a (both of them were measured at  $x=0.55Cr$ ), the inboard vortex formed on the leeward wing for S300000 is located nearer to the wing surface than that for S000000 because of the inboard vortex flap deflection. When compared to the results in Fig.4c and Fig.15b (both of them were measured at  $x=0.83Cr$ ), these figures show quite similar inboard vortex distributions. However, the outboard vortex of S300000 indicates weaker vorticity distributions when compared to that of S000000 (Fig.4c). The rolling moment hystereses are seen at around  $\phi=25^\circ$  at  $\theta=26^\circ$  in Fig.15. Further details of these hystereses should be investigated.

## 4 Conclusions

Wind tunnel measurements were done on a cranked arrow wing SST configuration with and without leading-edge flaps and leading-edge vortex flaps. The purpose of the measurements is to discuss the effect of leading-edge flap and vortex flap deflections on the static roll characteristics of the cranked arrow SST configuration.

1) Original wing without flap deflection indicates linear restoring moment for the roll direction at lower incidence angles  $\theta < 16^\circ$ . As the incidence angle increases, this linearity is lost. At  $\theta > 26^\circ$  the rolling moment drastically changes its state to an unstable one.

2) When the outboard leading-edge flap is deflected  $12^\circ$ , rolling moment hystereses are observed at the roll angle  $\phi$  of about  $20^\circ$  at the incidence angle  $\theta$  of about  $20^\circ$ . Cross flow velocity measurements at 83% chordwise position revealed that the vortex formed on the inboard wing does not break down until at a lower roll angle when the model is rolled in the counterclockwise direction (seen from downstream) than when the model is rolled in the clockwise direction. It was indicated that the vortex breakdown chordwise position on the inboard wing is different between when the wing is rotated in the clockwise direction and when it is rotated in the counterclockwise direction.

3) When the inboard leading-edge vortex flaps are deflected, the rolling moment characteristics are relatively similar to those of the original wing without flap deflections.

## References

- [1] Erickson G E. The Fluid Mechanics of Slender Wing Rock, *Journal of Aircraft*, Vol.21, No.5, pp 322-328, 1984.
- [2] Brennenstuhl U and Hummel D. Vortex Formation over Double-Delta Wings, Proceedings of 13th Congress of the International Council of the Aeronautical Sciences (ICAS Paper 82-6.6.3), Seattle, USA, Aug. 1982, pp.1302-1309.
- [3] Orsen P E and Nelson R C. Vortex Interaction Over Double Delta Wings at High Angles of Attack, AIAA Paper 89-2191, Jul. 1989.
- [4] Hanff E S and Jenkins S B. Large-Amplitude High-Rate Roll Experiments on a Delta and Double Delta Wing, AIAA Paper 90-0224, Jan. 1990.
- [5] Rao D M. Leading edge vortex-flap experiments on a 74deg. delta wing. NASA CR-159161, 1979.
- [6] Rinoie K and Stollery J L. Experimental studies of vortex flaps and vortex plates. *Journal of Aircraft*, Vol. 31, No. 2, pp 322-329, 1994.
- [7] Rinoie K, Fujita T, Iwasaki A and Fujieda H. Experimental studies of a 70-degree delta wing with vortex flaps. *Journal of Aircraft*, Vol. 34, No. 5, pp 600-605, 1997.
- [8] Rinoie K. Experiments of a 60-degree delta wing with rounded leading-edge vortex flaps. *Journal of Aircraft*, Vol.37, No.1, pp 37-44, 2000.
- [9] Rinoie K and Kwak D Y. Studies on vortex flaps having different flap hinge-line positions, *Journal of Aircraft*, Vol.38, No.2, pp 396-398, 2001.
- [10] Rinoie K, Miyata K, Kwak D Y and Noguchi M, Studies on Vortex Flaps with Rounded Leading Edges for Supersonic Transport Configuration, *Journal of Aircraft*, to be published. also ICAS 2002 8-7-3, 2002.
- [11] Kwak D Y, Miyata K, Noguchi M, Rinoie K and Fujita T, Roll Characteristics of the SST Configuration with LE Flap and TE flap at High Angles of Attack, AIAA Paper 2003-3413, Jun. 2003.
- [12] Sakata K. Supersonic Experimental Airplane (NEXST) for Next Generation SST Technology - Development and Flight Test Plan for the Unmanned Scaled Supersonic Glider, AIAA Paper 2002-0527, Jan. 2002
- [13] DANTEC. *FlowMap Installation & User's Guide*, Dantec Measurement Technology A/S, Denmark, 1997, pp 4.68-4.102.
- [14] The Visualization Society of Japan, ed. *PIV Handbook*, Morikita Shuppan, Tokyo, 2002, pp 137-164 (in Japanese).
- [15] Arena A S and Nelson R C. Unsteady Surface Pressure Measurements on a Slender Delta Wing Undergoing Limit Cycle Wing Rock, AIAA Paper 91-0434, Jan. 1991.
- [16] Grismer D, Nelson R and Ely W. The Aerodynamic Effects of Sideslip on Double Delta Wings, AIAA Paper 93-0053, Jan. 1993.
- [17] Jobe C E, Hsia A H, Jenkins J E and Addington A. Critical States and Flow Structure on a 65-Ddeg Delta Wing, *Journal of Aircraft*, Vol.33, No.2, pp 347-352, 1996.
- [18] Katz J and Levin D. Static Measurements of Slender Delta Wing Rolling Moment Hysteresis, *Journal of Aircraft*, Vol.28, No.4, pp 282-283, 1991.
- [19] Earnshaw P B. An Experimental Investigation of the Structure of a Leading-Edge Vortex, Aeronautical Research Council (ARC) Reports and Memoranda 3281, Mar. 1961.

[20] Visser K D, Iwanski K P, Nelson R C and Ng T T. Control of Leading Edge Vortex Breakdown by Blowing, AIAA Paper 88-0504, Jan. 1988.

[21] Gursul I and Yang H. On Fluctuations of Vortex Breakdown Location, *Physics of Fluids*, Vol.7, No.1, pp 229-231, 1995.

[22] Wentz W H, Kohlman D L. Vortex Breakdown on Slender Sharp-Edged Wings, *Journal of Aircraft*, Vol. 8, No. 3, pp 156-161, 1971.

[23] Verhaagen N G, Jenkins L N, Kern S B and Washburn A E. A Study of the Vortex Flow over a 76/40-deg Double-Delta Wing, AIAA Paper 95-0650, Jan. 1995.

[24] Ericsson L E. Effect of Angle of Attack on Roll Characteristics of 65-Degree Delta Wing, *Journal of Aircraft*, Vol.34, No.4, pp 573-575, 1997.

[25] Hebbar S K, Platzer, M F and Fritzelas, A E, Reynolds Number Effects on the Vortical Flow Structure Generated by a Double-Delta Wing, *Experiments in Fluids*, Vol.28, pp 206-216, 2000.

[26] Gursul I, Taylor G and Wooding C L, Vortex Flows over Fixed-Wing Micro Air Vehicles, AIAA Paper 2002-0698, Jan. 2002.

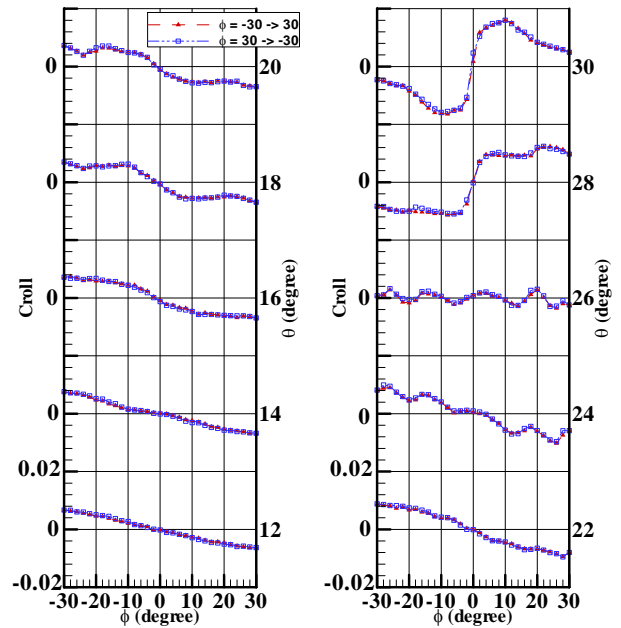


Fig.3 Rolling moment characteristics at different incidence angles, S000000

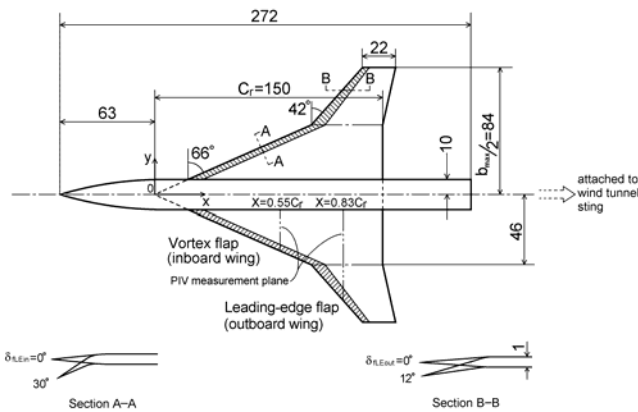


Fig.1 SST model, in millimeters

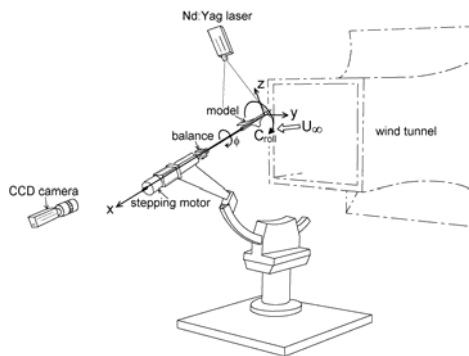


Fig.2 Experimental setup

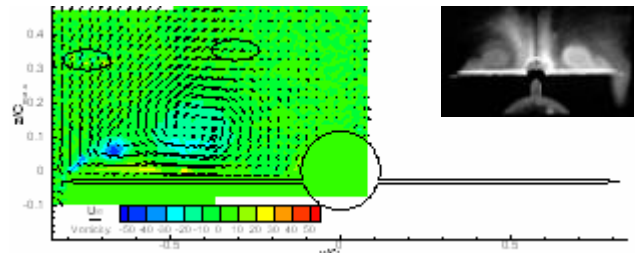


Fig.4a)  $\phi=0^\circ$

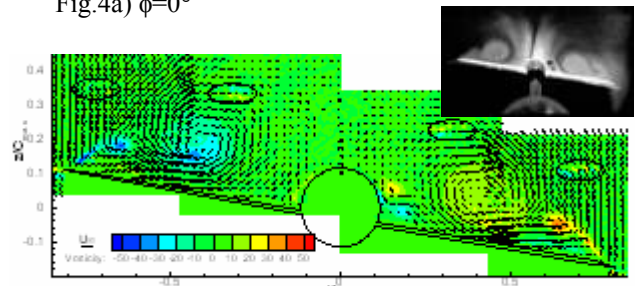


Fig.4b)  $\phi=10^\circ$

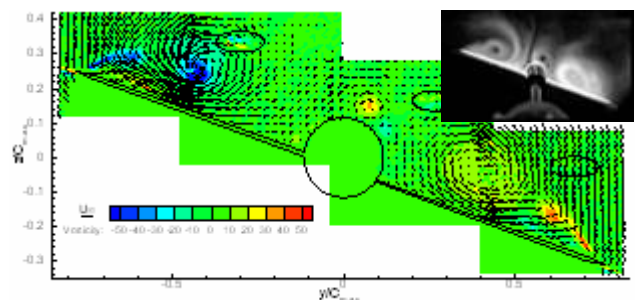


Fig.4c)  $\phi=20^\circ$

Fig.4 Cross flow velocity and vorticity distributions of S000000 at  $\theta=20^\circ$ ,  $x/ Cr=0.83$

**NON-LINEAR VORTEX BEHAVIOURS OF ROLLED SUPERSONIC TRANSPORT CONFIGURATION WITH LEADING-EDGE VORTEX FLAPS**

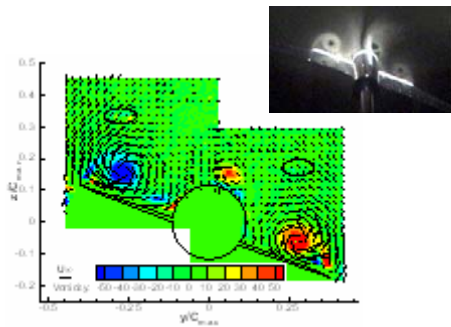


Fig.5 Cross flow velocity and vorticity distributions of S000000 at  $\theta=20^\circ$ ,  $\phi=20^\circ$ ,  $x/Cr=0.55$

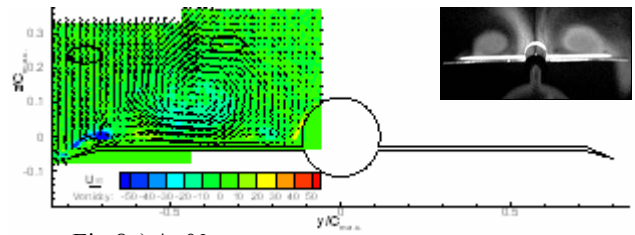


Fig.8a)  $\phi=0^\circ$

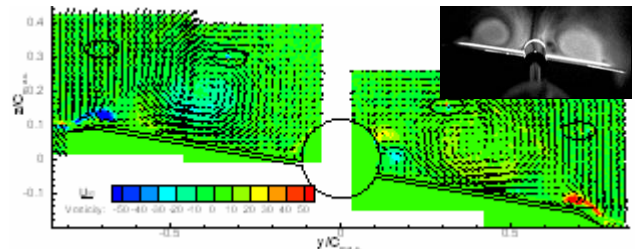


Fig.8b)  $\phi=10^\circ$

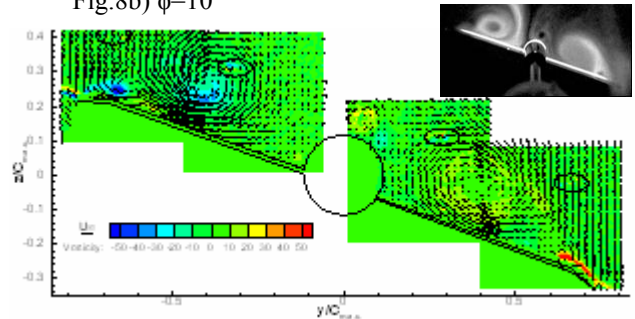


Fig.8c)  $\phi=20^\circ$

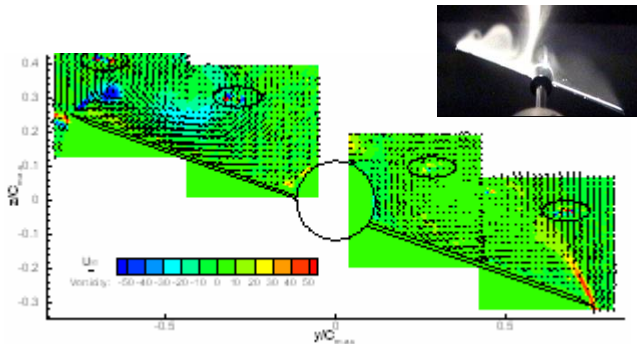


Fig.6 Cross flow velocity and vorticity distributions of S000000 at  $\theta=26^\circ$ ,  $\phi=20^\circ$ ,  $x/Cr=0.83$

Fig.8 Cross flow velocity and vorticity distributions of S001200 at  $\theta=20^\circ$ ,  $x/Cr=0.83$

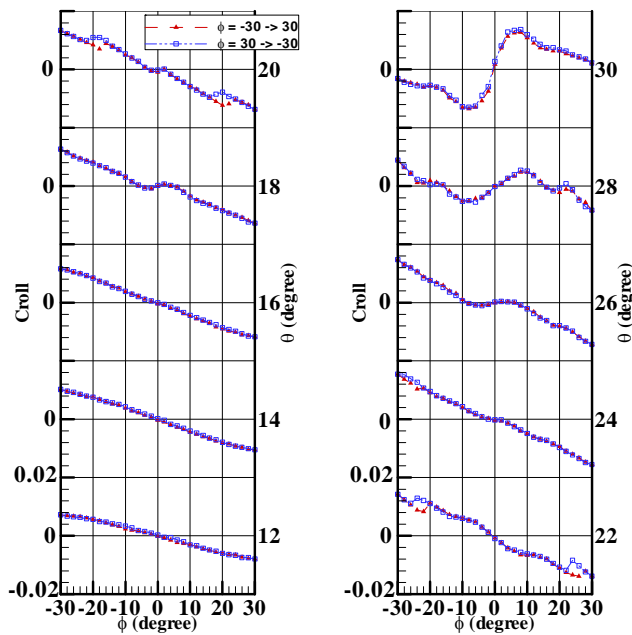


Fig.7 Rolling moment characteristics at different incidence angles, S001200

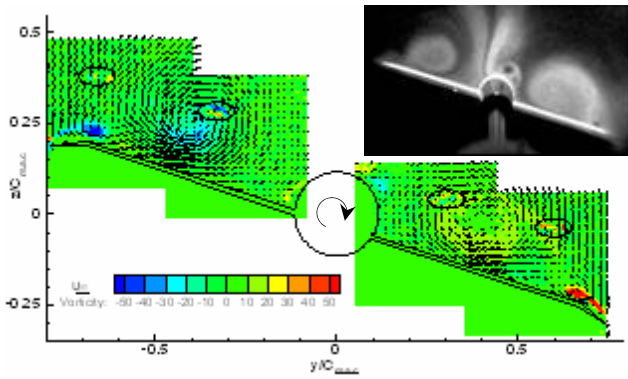


Fig.9a)  $\phi=18^\circ$  (clockwise)

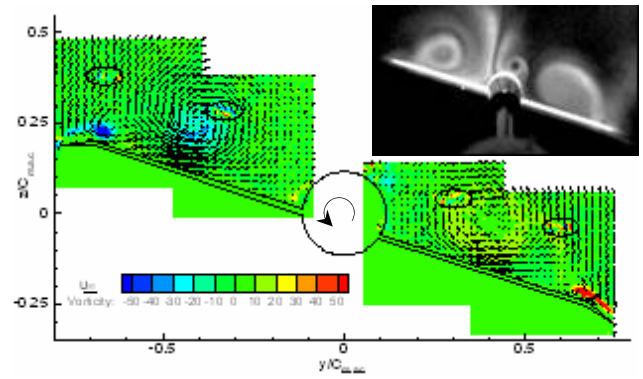


Fig.10a)  $\phi=18^\circ$  (counterclockwise)

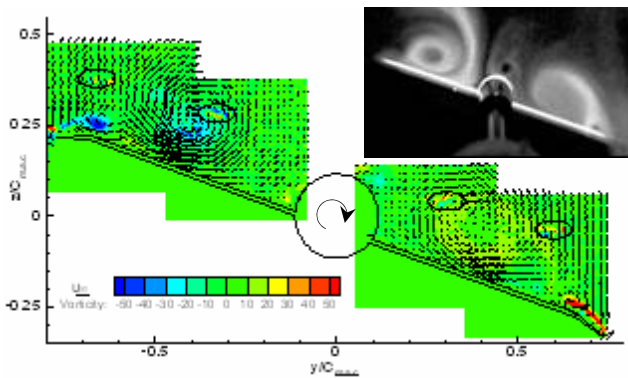


Fig.9b)  $\phi=20^\circ$  (clockwise)

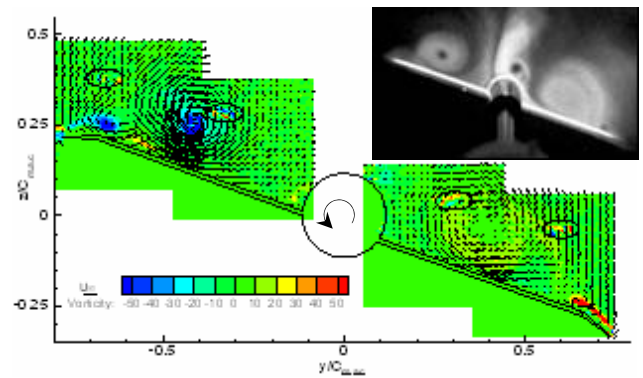


Fig.10b)  $\phi=20^\circ$  (counterclockwise)

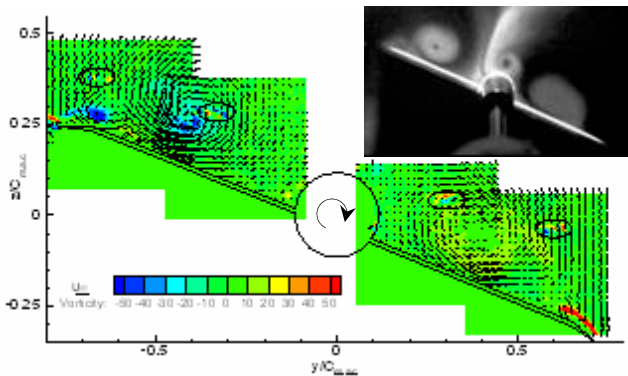


Fig.9c)  $\phi=22^\circ$  (clockwise)

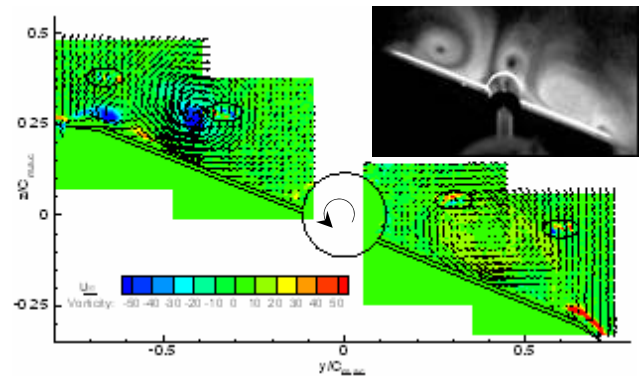


Fig.10c)  $\phi=22^\circ$  (counterclockwise)

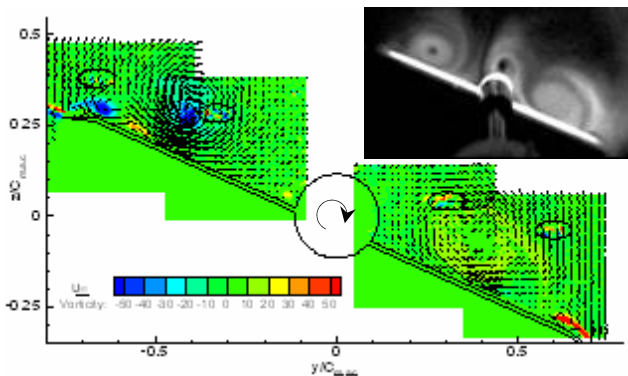


Fig.9d)  $\phi=24^\circ$  (clockwise)

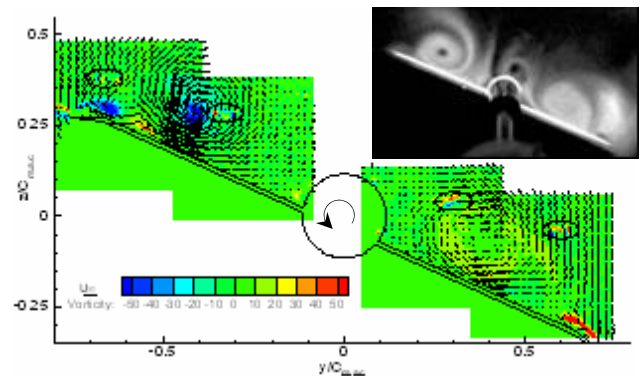


Fig.10d)  $\phi=24^\circ$  (counterclockwise)

Fig.9 Rolling moment characteristics at  $\phi=18^\circ$ - $24^\circ$ , clockwise rotation, S001200

Fig.10 Rolling moment characteristics at  $\phi=18^\circ$ - $24^\circ$ , counterclockwise rotation, S001200

## NON-LINEAR VORTEX BEHAVIOURS OF ROLLED SUPERSONIC TRANSPORT CONFIGURATION WITH LEADING-EDGE VORTEX FLAPS

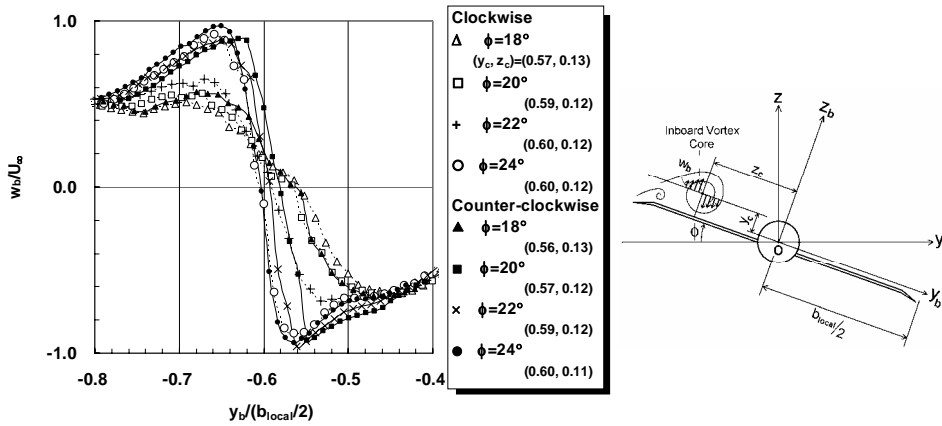


Fig.11  $z_b$ -component velocity  $w_b$  distributions along the parallel line to the wing surface that include the inboard vortex centre on the leeward wing of S001200 at  $\theta=20^\circ$ ,  $x/Cr=0.83$ .  $b_{local}$  is the span length at  $x/Cr=0.83$  without flap deflection

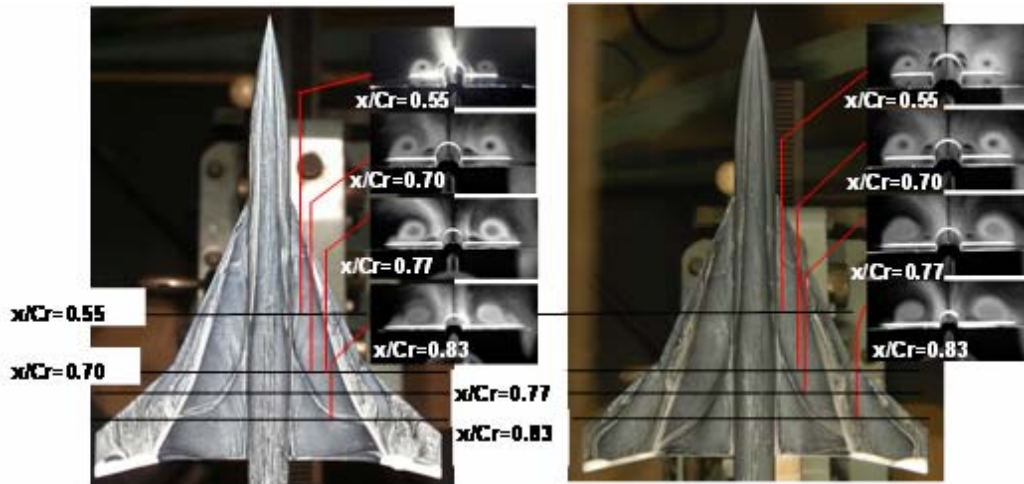


Fig.12a) S000000

Fig.12b) S001200

Fig.12 Oil flow and smoke visualizations at  $\theta=20^\circ$ ,  $\phi=0^\circ$

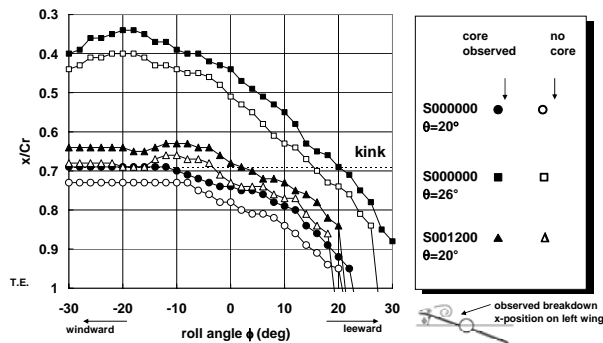


Fig.13 Effect of roll angle on vortex breakdown (S000000 at  $\theta=20^\circ$  and  $26^\circ$ , S001200 at  $\theta=20^\circ$ )

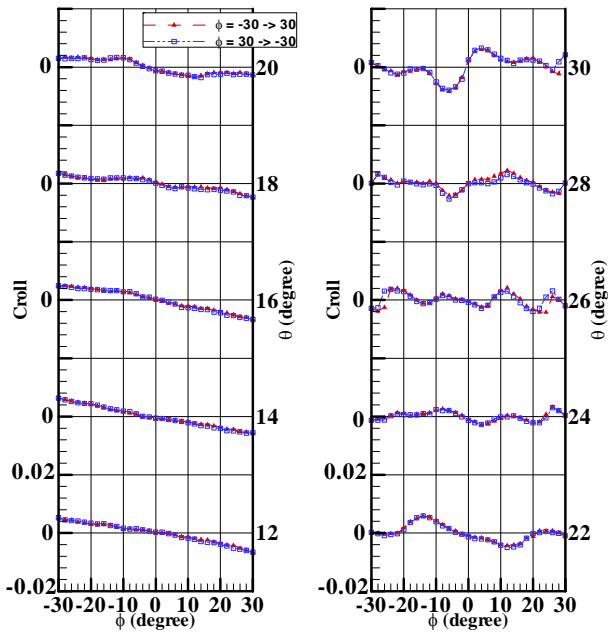


Fig.14 Rolling moment characteristics at different incidence angles, S300000

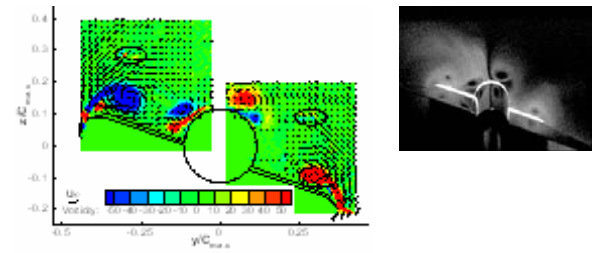


Fig.15a)  $x/ Cr=0.55$

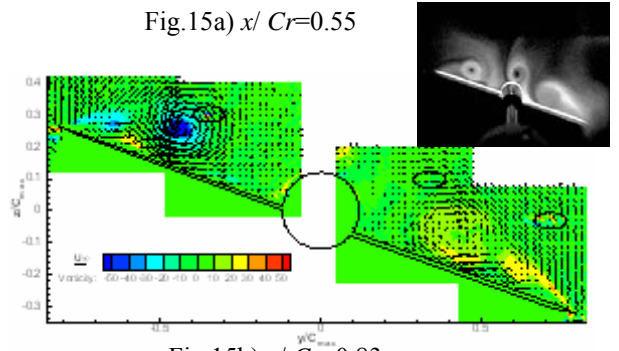


Fig.15b)  $x/ Cr=0.83$

Fig.15 Cross flow velocity and vorticity distributions of S300000 at  $\theta=20^\circ$ ,  $\phi=20^\circ$